Numerical Characterization and Experimental Optimization of Microfluidic DNA Microarray Hybridization

Parsa Sojoudi , Lin Wang , Paul C. H. Li *

Posted Date: 25 February 2026

doi: 10.20944/preprints202602.1306.v1

Keywords: computational simulation; mathematical modelling; DNA microarray; surface hybridization; convective/diffusive mass transport; microfluidic channel

 doi:10.20944/preprints202602.1306.v1

Article

Numerical Characterization and Experimental Optimization of Microfluidic DNA Microarray Hybridization

Parsa Sojoudi †, Lin Wang † and Paul C. H. Li *

Department of Chemistry, Simon Fraser University, Burnaby, BC V5A 1S6, Canada

* Correspondence: paulli@sfu.ca

† These authors contributed equally to this work.

Abstract

Background/Objectives: Mathematical modelling and computational simulation are important tools in the analysis of transport phenomena and surface reactions. These include surface hybridization that takes place in a microfluidic channel, creating a DNA microarray. **Methods**: In this work, the surface hybridization with multiple DNA probe spots immobilized on the bottom of a microfluidic channel was investigated using computational modelling. The model incorporates the 2D transport process, coupled with convective/diffusive mass transport (infinite dilution) and surface binding models for both non-specific adsorption and specific hybridization. **Results**: Hybridization signals obtained at different reaction times, various flow rates, and two different channel depths were analyzed, targeting enhanced surface hybridization while minimizing assay time and sample usage. It was found that a high aspect ratio (width/height) channel geometry with electrodes placed on the top and bottom walls would enable significantly improved fuel utilization and reduced inter-diffusional mixing width. **Conclusions**: The numerical study also suggested the implementation of a tapered electrode design that accommodates the growth of the co-laminar mixing zone in the downstream direction.

Keywords: computational simulation; mathematical modelling; DNA microarray; surface hybridization; convective/diffusive mass transport; microfluidic channel

1. Introduction

Like other biosensor technologies, the DNA microarray is based on the fundamental property of nucleic acid strands specifically binding (hybridizing) to their complementary strands [1]. Generally, probe DNA molecules are immobilized on a solid surface and form an array of microspots. Then, labelled target DNA strands in the solution phase are applied to the surface. Since the immobilized probe DNA binds to, and hence retains, its complementary target strand, detection is achieved through the read-out of the fluorescent markers tagged on the retained target molecules.

The conventional microarray method occurs in a static mode, where sample DNA molecules in bulk solutions are transported to the reactive surface solely through slow molecular diffusion. This slow process could limit the rate of the hybridization, leading to a poor detection efficiency that may be resolved by using a long incubation time (12-18 h) [2]. The recent microfluidic technology enhances the mass transport by introducing convection to the microarray system [3,4]. Moreover, the microfluidic method shows the advantages of low sample usage (down to submicrolitre) and reduced assay time (in minutes), as compared to the conventional bulk solution method [5].

The kinetics of DNA microarray hybridization, which is heterogeneous, is much more complex than that of homogeneous liquid-phase DNA hybridization [6,7]. Other than the hybridization rate, additional parameters from the mass transport mechanism, such as bulk and surface diffusivity, flow velocity, channel geometries, etc., are involved. A sound and detailed mathematical modelling of the

 doi:10.20944/preprints202602.1306.v1

concurrent diffusion and reaction processes is thus needed to fully understand both convection and diffusion processes in the DNA microarray system. Since the system shares many features with the heterogeneous interactions of other biosensors, whose theoretical studies have provided considerable insight into the process of DNA surface hybridization. For example, a simplified two-compartment model was originally proposed for the surface antigen-antibody reaction in protein biosensors [8–13], and this model was then used to analyze the on-chip DNA hybridization [14,15]. A diffusion-reaction model was developed for a cell receptor-ligand model [16], and it was first used by Chan et al. to study static microarray hybridization [17,18]. In this study, hybridizations of DNA targets both from the bulk phase and from initial non-specific surface adsorption were considered, and the model successfully predicted the enhanced kinetics due to sparse surface probe coverage. Other models have also been reported to further describe the effect of different physico-chemical parameters on kinetics during static hybridization [19–21]. Regarding hybridizations in microfluidic channels, Erickson et al., who coupled Chan's work with convection transport relations, examined their model with experimental results obtained from oligonucleotide targets introduced in microchannels [22]. Similar models have been reported for other microfluidic-based surface biosensors [23–25]. Because the mathematical description of these models involves the use of nonlinear partial differential equations, numerical solutions have been achieved only with the increasing computing power of modern computers [15,22,24–26].

Our present work aims at providing a thorough analysis of the combined effect that the many different process variables have on DNA microarray hybridization in diffusion- and convection-driven systems. The use of dimensionless parameters and variables in our work brings in a universal character to the model, transforming a specific situation into a generic case, as it has been applied in a few studies on static hybridization [27,28]. The proposed model was solved numerically, and the results have been used to predict the detection limit of single-stranded targets and to examine the effects of flow rate, channel depth and probe density on hybridization kinetics. The predicted results were validated with experimental data. Our work provides a means for the experimentalists to estimate the importance of different parameters involved in a microfluidic microarray chip and to use these parameters to aid their design process.

2. Materials and Methods

2.1. Model Systems

The configuration of a rectangular microchannel in a polymer microchip is shown schematically in Figure 1a. The liquid inside the channel is assumed to flow at a steady state (in x direction) in the absence of body forces like gravity. Since the width of a rectangular channel (in y direction) is larger than the channel height (in z direction), an infinite parallel-plate configuration is a reasonable approximation of the channel. The y coordinate is thus dropped out, and 2-D geometry (x-z) is used (Figure 1b). By solving the Navier-Stokes equation, which describes the flow behaviour of the fluids in a channel, the 2-D flow profile in the channel can be described by a parabola given by equation 1 as follows:

$$u = 6U\frac{z}{H}\left(1-\frac{z}{H}\right) \tag{1}$$

where u is the flow velocity at z, U is the average flow velocity, and H is the height of the channel. Both U and H can be measured experimentally. On the other hand, the bulk-phase transport of DNA target molecules in the 2-D channel flow can be described by the convection-diffusion equation as follows:

 doi:10.20944/preprints202602.1306.v1

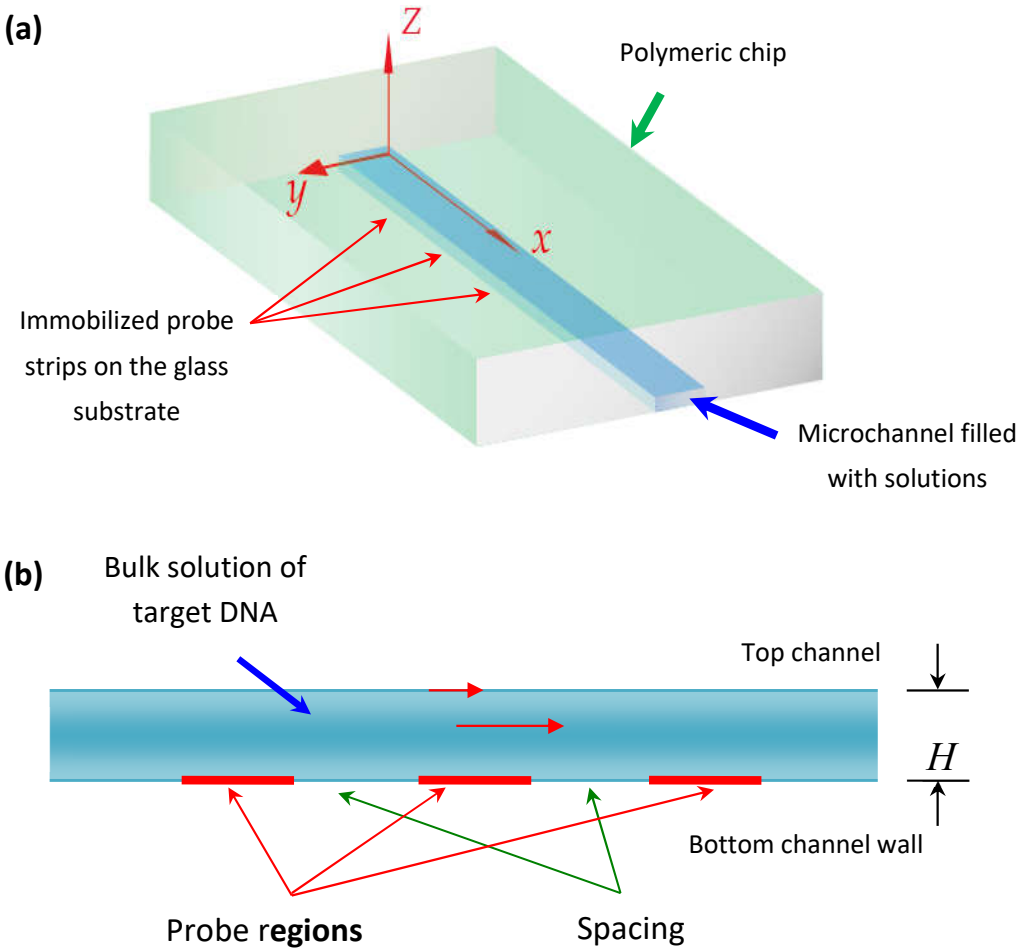

Figure 1. (**a**) A polymeric chip with a rectangular microchannel filled with solutions. The bottom wall of the microchannel is immobilized with 3 probe strips; (**b**) The simplified 2-D geometry (in the x-z directions) of the above microchannel was used for the model construction and numerical simulation. The two diagrams are not drawn to scale.

$$\frac{\partial C}{\partial t} = D\left(\frac{\partial^2 C}{\partial x^2} + \frac{\partial^2 C}{\partial z^2}\right) - u\frac{\partial C}{\partial x} \quad (2)$$

where C is the target concentration in the bulk solution, and D is the diffusion coefficient of the DNA molecules in the bulk phase.

Three surface-phase processes have been considered in the model construction relevant to the heterogeneous hybridization of target DNA in the microchannel. Eqn. (3) describes the bulk-to-surface DNA hybridization reaction to the immobilized DNA probes. Eqn. (4) describes the nonspecific adsorption of target DNA molecules from the bulk phase to the glass substrate. These nonspecifically adsorbed DNAs can then hybridize to the immobilized probe, as shown in Eqn. (5).

$$\text{Target DNA (in bulk phase)} + \text{Probe DNA (immbolized)} \underset{k_{-3}}{\overset{k_3}{\rightleftharpoons}} \text{Hybridized Duplex} \quad (3)$$

$$\text{Target DNA (in bulk phase)} \underset{k_d}{\overset{k_a}{\rightleftharpoons}} \text{Target DNA (adsorbed on the surface)} \quad (4)$$

$$\text{Target DNA (adsorbed on the surface)} + \text{Probe DNA (immbolized)} \underset{k_{-2}}{\overset{k_2}{\rightleftharpoons}} \text{Hybridized Duplex} \quad (5)$$

 doi:10.20944/preprints202602.1306.v1

where k_3 and k_{-3} represent bulk-to-surface hybridization and dehybridization constants, respectively; k_2 and k_{-2} represent surface-to-surface hybridization and dehybridization constants, respectively; k_a and k_d represent the nonspecific adsorption and desorption constants, respectively.

Therefore, the temporal variations of the hybridized DNA (Θ) and the non-specifically adsorbed DNA (η) can be described as:

$$\frac{\partial \Theta}{\partial t} = \left[k_3 C_w \left(\Theta_0 - \Theta\right) - k_{-3}\Theta\right] + \left[k_2 \eta \left(\Theta_0 - \Theta\right) - k_{-2}\Theta\right] \quad (6)$$

$$\frac{\partial \eta}{\partial t} = D_s \nabla^2 \eta + \left[k_a C_w \left(\eta_{\max} - \eta\right) - k_d \eta\right] - \left[k_2 \eta \left(\Theta_0 - \Theta\right) - k_{-2}\Theta\right] \quad (7)$$

where C_w is the bulk concentration of DNA target adjacent to the bottom wall (z = 0), Θ is the surface concentration of the hybridized duplexes, Θ_0 is the maximal surface concentration of hybridized duplexes and it is equal to the probe density, (Θ_0 - Θ) is the concentration of the available probe molecules on the surface, η is the surface concentration of non-specifically adsorbed target DNA molecules, and D_s is the surface diffusion coefficient of the target DNA on the glass substrate.

The surface DNA concentration due to adsorption (η) and hybridization of the target DNA to a surface-immobilized probe (Θ) was coupled to the convection-diffusion equation by a flux balance at the wall:

$$-D\frac{\partial C(x,z,t)}{\partial z}\Big|_{z=0} = \left[k_a C_w \left(\eta_{\max} - \eta\right) - k_d \eta\right] + \left[k_3 C_w \left(\Theta_0 - \Theta\right) - k_{-3}\Theta\right] \quad (8)$$

2.2. Computational Simulations

Numerical simulations for the hybridization fraction (Θ*) and its visualization were performed with COMSOL Multiphysics 3.5a under the assumption of unidirectional 2-D pressure-driven flow.

3. Results

3.1. Detection Limit

The detectable concentration range of target DNA depends upon the performance of both the microarray sensor and the fluorescent scanner. Although modern scanners usually have a 16-bit digitization in signal outputs or a dynamic range of 2^{16} or 65, 536, the actual dynamic range is less than 5 orders of magnitude [29]. It is because the detection range is confined by the probe density (upper limit) as well as the detection limit of the scanner (lower limit).

In our model of DNA hybridization, we have estimated that the probe density (Θ_0) on the aldehyde-modified glass surface is ~ 5×10^{11} strands/cm^2 or 8.3×10^{-9} mol/m^2 [30]. This probe density is comparable to the values obtained elsewhere [31–36]. On the other hand, for the Typhoon 9410 fluorescence scanner, the limit of detection of Cy5 labels is 200 amol per ~5 mm^2 area[30], or ~ 4×10^{-11} mol/m^2, which is taken as Θ_{min}. In its dimensionless form, the minimum detectable fraction Θ^*_{min} (= Θ_{min} / Θ_0) is 0.005. The use of dimensionless parameters and variables in our work brings in a universal character to the model, transforming a specific situation into a generic case, as it has been applied in a few studies on static hybridization [27,28].

Now, the detection limit of the DNA sensor can be estimated from Θ^*_{min}. Assuming no non-specific adsorption ($k_2 = k_{-2} = 0$) and no target depletion ($C_{z=0} = C_0$) for simplicity, the hybridization fraction Θ* (defined as Θ/Θ_0.) can then be calculated by solving equation (6) to give

$$\Theta^* = \frac{\Theta}{\Theta_0} = \frac{C_0/K_3}{1 + C_0/K_3} \cdot \left(1 - e^{-(k_3 C_0 + k_{-3})t}\right) \quad (9)$$

where K_3 is defined as k_3/k_{-3}.

At equilibrium (i.e. t = ∞ in eqn. 9), the fraction of hybridized DNA duplex, Θ^*_{eq}, is given by

$$\Theta^*_{eq} = \frac{C_0}{K_3 + C_0} \quad (10)$$

 doi:10.20944/preprints202602.1306.v1

The detection limit of the DNA sensor (or minimal detectable bulk concentration) can be estimated by using the equilibrium concentration (Θ^*_{eq}) for Θ^*_{min}. Since Θ^*_{min} is much less than 1, the detection limit of the sensor is approximately equal to $K_3\Theta^*_{min}$. Since k_3 was measured to be ~1×105 $M^{-1}\cdot s^{-1}$ and k_{-3} to be ~2×10^{-4} s^{-1} [66], for room temperature hybridization of 20-mer oligonucleotides with 20-mer immobilized probes, the value of K_3 for the hybridization of 20-mer oligonucleotides with 20-mer immobilized probes at room temperature was calculated to be 2 nM. Since Θ^*_{min} is 0.005 using the Typhoon scanner, the detection limit of the DNA sensor will be 10 pM (i.e. $K_3\Theta^*_{min}$ = 2.5 nM · 0.005 = 10 pM) for room temperature hybridization of 20-mer oligonucleotides with 20-mer immobilized probes. This detection limit will be lower for shorter oligonucleotides because of a lower value of K_3.

3.2. Reaction Time

The time scale for the DNA sensor to reach the minimal detectable surface fraction (Θ^*_{min}) can be estimated from the hybridization kinetics curves described by equation (9). Figure 2 shows the plots of the surface hybridization of the DNA sensor with a target concentration range from 1 pM to 1 μM. The detection of DNA targets can be fast. For instance, for 1-nM oligonucleotide targets, the hybridization signal can be detected in 30 s (i.e. the time needed to reach Θ^*_{min} of 0.005). This prediction is consistent with our observation of 3-min detection of 1 nM DNA targets (ref). On the other hand, for a more diluted target solution at 0.1 nM or 100 pM, a minimal reaction time of 300s is needed for reliable detection.

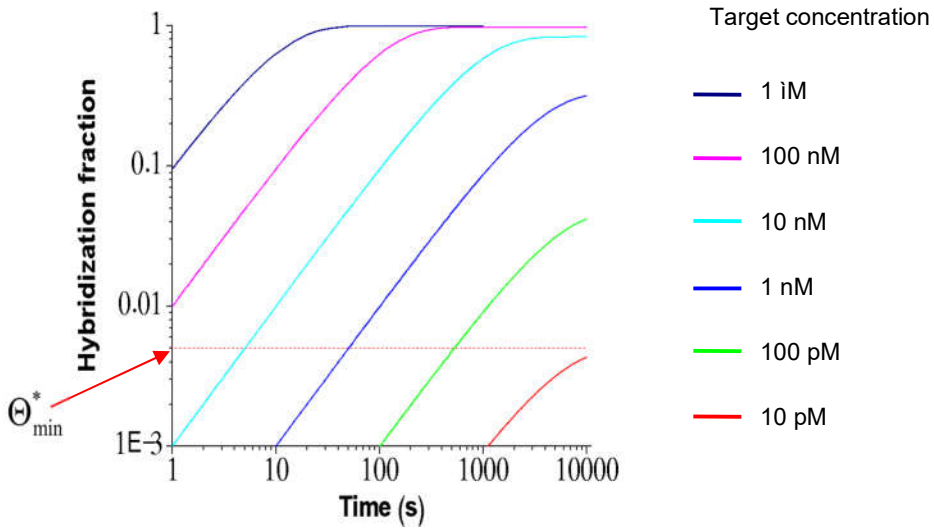

Figure 2. Kinetics curves of DNA surface hybridization. The bulk concentrations of DNA targets range from 10 pM to 1 μM. The red dotted line represents the minimal detectable hybridization fraction (Θ^*_{min} = 0.005) limited by the fluorescence scanner. For instance, it takes 30 s for 1 nM to reach 0.005.

Since the detection limit of the DNA sensor depends on the kinetic constant of hybridization (k_3 and k_{-3}), the sensing performance can be improved by optimizing hybridization kinetics by adjusting experimental conditions, such as ionic strength, target sequence, and probe density. For example, Studier et al. found that the hybridization rate in low-salt concentration (<1.0 M) is proportional to the cube of [Na+] [37], and so this effect of salt concentration (0.15M and 0.6M) has been included for simulation.

As seen in the simulated results in Figure 3 (a), the hybridization fraction is greater in the 4X SSC buffer ([Na+] = 0.6 M); it is well known that a high ionic strength buffer usually results in higher hybridization signals.

In DNA microarray applications, the surface-immobilized probe molecules are usually oligonucleotides with lengths varying from 20 to 30 bases [63–65]. However, the sample target DNA

 doi:10.20944/preprints202602.1306.v1

strand can be of any length; it could be as long as the immobilized probes, or it could be longer, such as 50-mer or longer in PCR products. The dangling ends of the target DNA after hybridization have been reported to have a stabilization effect on the DNA duplex [39]. The hybridization free energy change can be calculated using the nearest-neighbour model (ref). We applied this model to calculate the free energy changes (ΔG) for the two different duplexes resulting from either 22-mer or 50-mer targets. The value of ΔG is mainly manifested in the dehybridization rate constant (k_{-3}) that goes in the simulation for Θ*. From Fig. 3b, it can be seen that hybridization fraction has an increase of 2-3-fold for the 50-mer target DNA, especially at the low target concentration, and this increase implies a lower detection limit. The simulated results are consistent with the experimental data. For instance, the hybridization fraction of 0.01 nM of the 50-mer target is 0.01, which is higher than that from the 22-mer target (0.002).

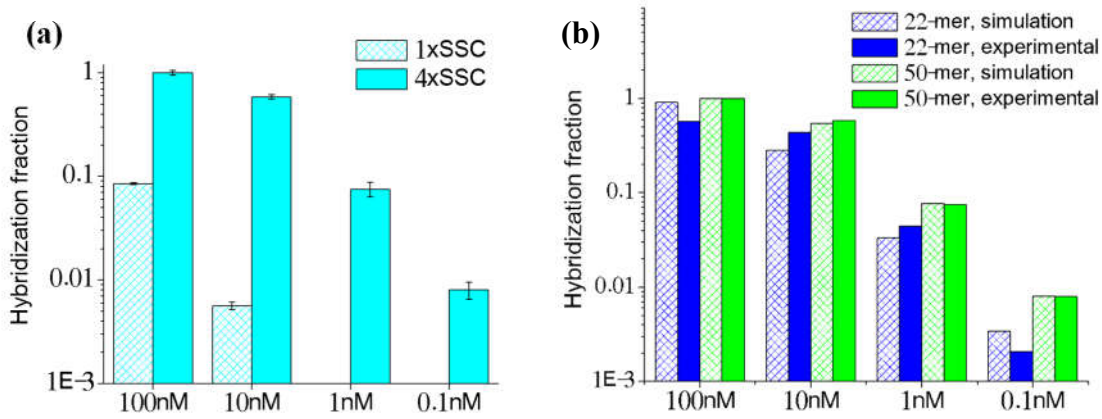

Figure 3. Effects of salt concentration and target length. **(a)** Hybridization fraction simulated at two salt concentrations, 0.15M and 0.6 M NaCl in 1X SSC and 4X SSC, respectively. **(b)** Hybridization fraction simulated and observed at two target lengths. The probe sequence length is fixed at 22-mer.

3.3. Probe Density

The sensing performance of a DNA microarray depends on the probe density in two opposing ways. First, the higher the probe density is, the higher the hybridization fraction as well as the maximum hybridization signal is. Second, the kinetics of the hybridization process is affected by a higher probe density. The current view of duplex formation for short oligonucleotides is nucleation first, followed by fast zipping [40]. For the target DNA molecule to hybridize to the probe immobilized at the surface, it has to first penetrate into the probe DNA film. Therefore, it is possible that lateral steric interactions with nearby probe DNA molecules affect the hybridization kinetics. In fact, surface hybridization of tightly packed probe molecules has been reported to be less efficient than that of loosely-packed probes [32,41,42].

The effect of probe density on hybridization signals was evaluated by simulation. Here, an equation proposed by Chan et al. was used to estimate the relationship between probe density and the kinetic constant k_3 [17]. The equation is shown as follows:

$$k_3 = \frac{DN_A \pi R_p^{\,2} \chi_3}{\sigma_3} \tag{11}$$

where D is the diffusion coefficient; NA is the Avogadro constant; χ_3 is the reaction success probability, and it is chosen to be 0.001 [17]; σ_3 is the persistence length of the target DNA; *Rp* is the radius each probe molecule may cover; which is calculated using the following equation by assuming there is no overlap of probe molecules in the sensing region [17]:

$$R_p = \frac{1}{2}\sqrt{\frac{1}{N_A \Theta_0}} \tag{12}$$

 doi:10.20944/preprints202602.1306.v1

where N_A is Avogadro's constant; Θ_0 is probe density.

From Eqn 11, for the same DNA targets, the kinetic constant of surface hybridization (k_3) is inversely proportional to the surface probe density (Θ_0). This relationship has been confirmed experimentally by the work of Michel *et al*., who found that with probe density decreased by four times from 5.2×10^{11} to 1.38×10^{11} strands/cm^2, the value of k_3 increases almost four-fold from 0.9×10^5 to 4.3×10^5 M^{-1}·s^{-1} [42]. On the other hand, the reaction rate of dehybridization (k_{-3}) did not change significantly with the change of Θ_0 from the experimental findings in Michel *et al*.'s work [42]. Therefore, an assumption that the k_{-3} remains constant for different values of Θ_0 is reasonable, and this assumption is used in our subsequent simulations.

Figure 4a shows both simulated and experimental results of the effect of probe density on the hybridization fraction. As described in our previous work, the probe density on a glass slide was controlled by using different concentrations of probe solutions during the printing procedures [30]. The resulting probe densities vary from 2.3×10^{11} to 7.9×10^{11} strands/cm^2, which are comparable to the values obtained in the studies by other groups [31–36]. As seen in Figure 4a, although the probe density increased by almost 4 times, the hybridization intensities from experimental measurements increased by only ~ 1.5 times. Moreover, no significant increase in hybridization signals was observed when the probe density was higher than 5.4×10^{11} strands/cm^2. The simulation results are comparable to the experimental findings. The hybridization intensity increased by ~2 times, and it reached a plateau after the probe density is higher than 4.7×10^{11} strands/cm^2.

The observation that the simulated results give a higher hybridization ratio, as compared to the experimental findings, could be attributed to the setting of the reaction success probability, χ_3, in equation (11). Though it was chosen as 0.001 during simulation, it could be lower for diluted target solutions [17].

Since the kinetic constant of surface hybridization (k_3) is inversely proportional to probe density, the lowest probe density will result in the fastest hybridization. This is shown in Figure 4b, and the signals are further enhanced when a longer hybridization time is used. The simulated hybridization fraction (Θ^*) can reach a saturated level in the given time (i.e. 100 s) when the probe density is the lowest at 2.3×10^{11} strands/cm^2. However, with the increasing probe density, the rate of the increase of Θ^* is reduced significantly, and it does not reach saturation within 180 s.

In order to compare the hybridization signal at different probe densities, one has to multiply Θ^* by the corresponding probe density. Although a higher probe density can provide a higher surface concentration of unhybridized probe molecules, this effect could counteract the effect of a lower k_3 value at higher probe density, and these 2 opposing effects result in the plateau shape in Figure 4a.

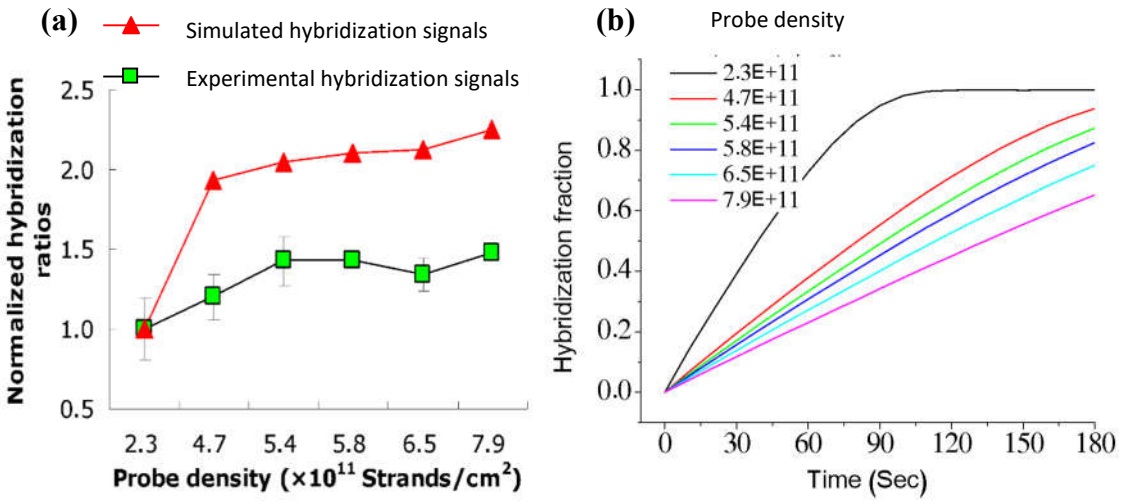

Figure 4. (**a**) The experimental and simulation results of the effect of probe coverage on hybridization signals. The top curve with triangle labels shows the simulated hybridization fractions at different probe densities; the

 doi:10.20944/preprints202602.1306.v1

bottom curve with square labels shows the corresponding hybridization signals obtained experimentally with 22-mer targets. (**b**) The simulated kinetic curves of hybridization at different probe densities.

3.4. Surface Hybridization with Mass Transport Limitation Due to Diffusion

In contrast to solution-phase hybridization, probe molecules in microarray analysis are immobilized on a solid surface, and so the target molecules in the bulk phase have to be transported to the surface probe region by diffusion before hybridization. This diffusion process is slow due to the slow diffusion of DNA molecules [3,15,23,43–46], and so there are usually insufficient signals in microarray analysis unless the reaction time is long enough or a convective flow is introduced. The microfluidic microarray method, which introduces additional mass transport for DNA target molecules through flow convection, can thus alleviate the diffusion limitation in microarray signals.

Figure 5a shows the simulated kinetic curves for hybridization conducted under a static or stop-flow (static) condition and a microfluidic flow (microfluidic) condition. The average signal obtained at 3 min. from the flow method (1 mm/s) is ~ 3 times as high as that obtained from the static method. By solving equation (8) numerically, the profile of the bulk concentration (C) after 3 minutes. static or microfluidic hybridization of oligonucleotide targets is shown in Figure 5a insets. It can be seen that the target DNA concentration is already consumed to a larger extent along the bottom wall during static hybridization. The calculated sample concentration at the bottom wall (C_w) adjacent to the no-probe regions drops drastically from 10 nM to 8.3 nM. This decrease in bulk concentration is due to the non-specific adsorption of target molecules on the glass surface. At the probe regions, the hybridization process significantly depletes C_w down to 1.2 nM. On the contrary, microfluidic flows prevent localized target depletion around the probes by continuous replenishment with fresh sample target solutions. The lowest concentration of bulk solution at the bottom wall (C_w) is still high at 9.6 nM after 3-min hybridization. Higher local target concentration achieved in the microfluidic flow results in faster mass transport and hence faster hybridization kinetics.

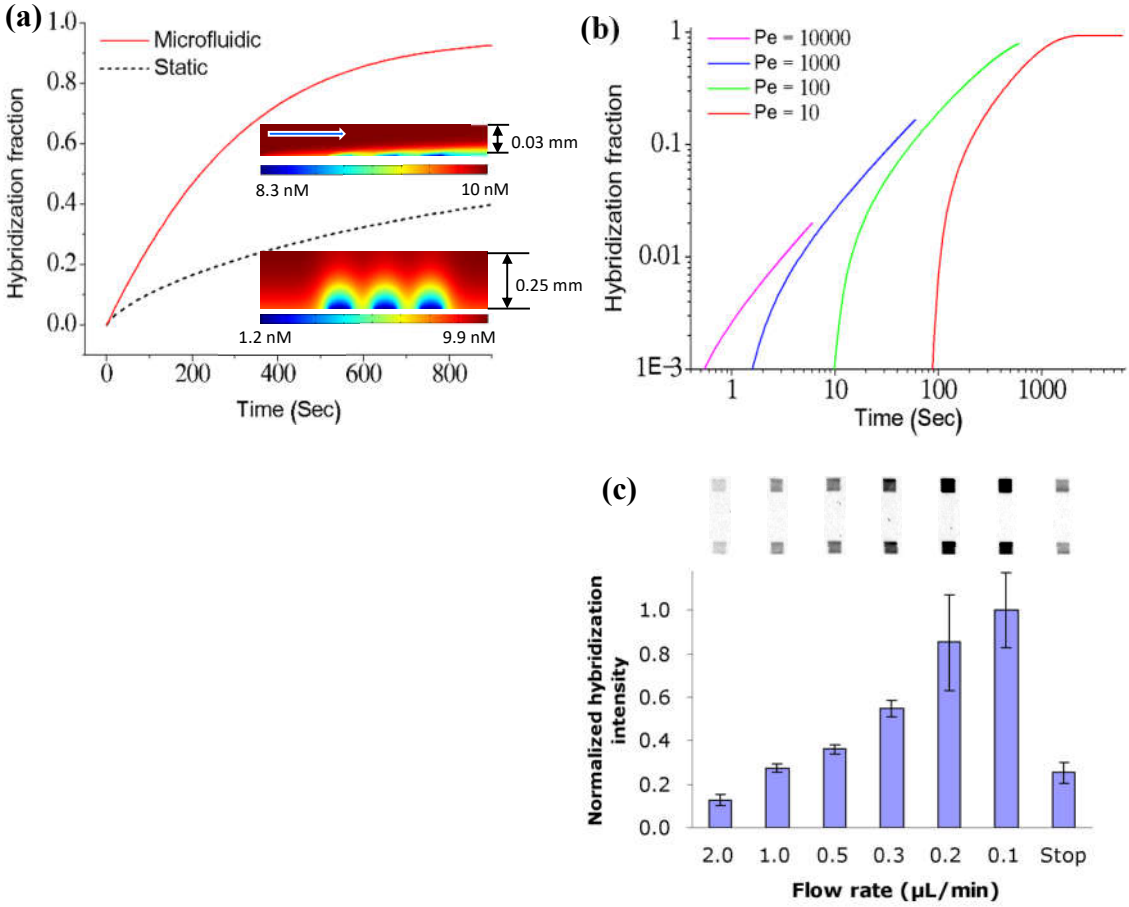

 doi:10.20944/preprints202602.1306.v1

Figure 5. The effect of mass transport limitation on the sensor performance. (**a**) Kinetic curves showing the change of the hybridization fraction vs. time during the static or microfluidic hybridization in 15 min. The initial target concentrations are 10 nM, and the average flow velocity is 1 mm/s in the microfluidic method. The two insets show the bulk concentration profiles after 3 min. (or 180 s) of microfluidic hybridization (top) or static hybridization (bottom). In both images, an array of 3 probe spots has been incorporated in the model. The probe region width and spacing are 200 μm. The bottom rainbow bars denote the scale of the bulk concentration. (**b**) The simulated hybridization kinetics at different flow conditions. In the dynamic flow method, four flow speeds of 0.01 to 1 mm/s (from left to right) have been simulated, and the corresponding Pe values are from 10 to 10000. 1 μL of 10-nM oligonucleotide samples was applied to each microchannel. (**c**) The hybridization intensities (normalized to the intensity obtained at 2.0 μL/min) from the microfluidic method were conducted at different flow rates (2.0, 1.0, 0.5, 0.3, 0.2, and 0.1 μL/min). For comparison, the data in the rightmost column is from the 30-min static or stop-flow hybridization. 1 μL of 10-nM oligonucleotide samples was applied to each microchannel. The error bars are from the standard deviation of 5 hybridization patches.

3.5. Flow Rate

The effect of flow rates on hybridization kinetics was further studied in this work. The dimensionless Péclet number (*Pe*), which is the ratio between the characteristic convection rate and diffusion rate, is used to evaluate the effect of flow. When $Pe \gg 1$, the convective transport dominates over diffusion, and so the localized depletion is eliminated, resulting in a reaction-limited, but not diffusion-limited, hybridization. A high *Pe* number can be readily achieved by flushing the target solution through the hybridization channel at a high flow speed. However, at a fixed hybridization time, a faster flow will result in a larger sample consumption compared to a slower flow, unless some recirculation facilities are used to reduce the sample consumption [46–48]. On the other hand, when the sample volume is fixed, the total residence time decreases at high flow rates, and the hybridization signal could be reduced. It is thus important to identify the optimal flow rate for the quantification of microfluidic DNA hybridization within small sample volumes.

Since the sample volume is fixed to 1 μL, the reaction time (from 6000 s to 6 s) is inversely proportional to the flow rate (from 0.01 to 10 μL/min, respectively). Figure 5b shows the simulated hybridization fractions (Θ^*) at different flow speeds. The highest hybridization fraction is found at the lowest flow speed ($Pe = 10$). Nevertheless, the assay time is too long in this case (~6000 s), and the maximal signal occurs at an impractically long time of ~2000 s; this approach is even worse for large sample volumes [49]. It is also found that the benefit of hybridization enhancement is marginal if obtained from a very slow flow speed. For example, a 10-fold decrease in the flow speed from $Pe = 10000$ to $Pe = 1000$ results in a ~10-fold increase in the hybridization fraction. However, if the flow speed decreases at the same ratio from $Pe = 100$ to $Pe = 10$, the increase in the hybridization fraction is less than 2-fold, and this is obtained at the expense of a 10-fold increase in reaction time. Therefore, the optimized flow speed with the consideration of both the reaction time and hybridization signal intensities is to be found at around $Pe = 100$, where the average flow speed is between 0.1~1 mm/s and the hybridization time is at the level of 10 min using the 30-μm deep microchannel in the experiment.

We performed experiments to identify the effects of flow rates on the hybridization signals. The same amount of oligonucleotide target solutions (1 μL) was introduced to the probe region by either static stop-flow or dynamic flow. In the static method, the hybridization time was set to 30 min, while the actual hybridization time in the latter method depends on the flow rate used. For instance, the hybridization time of 1 μL at 0.1 μL/min was 10 min. The resulting fluorescence images and signals are shown in Figure 5c. As expected, it is found that the diffusion-limited static hybridization does not give a strong signal even though the hybridization time of 30 min. is the longest. In terms of the dynamic hybridization, the flow with the lowest flow rate (0.1μL/min, $Pe = 100$) gave the highest hybridization signals, indicating the reaction is not diffusion-limited. For the flow hybridization at the highest flow rate (2 μL/min, $Pe = 2000$), although the mass transport is least likely to be diffusion-limited, it resulted in the lowest hybridization signal, probably because of a low residence time for reaction.

 doi:10.20944/preprints202602.1306.v1

3.5. Effect of Channel Depth

The reduction of channel height is another strategy to efficiently deliver target molecules to the surface probes [50–53]. At the same flow speeds, the shallower microchannel results in a longer residence time as compared to the deeper channel. The increase of hybridization signals is thus expected due to longer reaction time in the shallower microchannels. On the other hand, if the total residence time is controlled to be the same for both types of microchannels, the flow speed in shallower microchannels is thus higher, which increases the convective flux (from higher flow speed). Moreover, the characteristic diffusion time of target molecules in shallow channels is less than that in deep channels, which will also benefit the surface hybridization. As seen from Figure 6a, the simulated hybridization signal increases by 17% by decreasing the channel depth from 75 μm to 24 μm. As compared to the experimental findings, the increase of hybridization signals from shallower microchannels is even higher at ~100%. This discrepancy could be due to the further improvement from the stabilization effect on hybridized DNA induced by microflow, i.e. the increase of flow speed might benefit duplex formation [54,55].

On the other hand, the reduction of channel height shows an adverse effect on static microarray hybridization. From the simulation results shown in Figure 6a, the hybridization signal decreases by ~75% with the shallow microchannel when using the stop-flow method. This is understandable because fewer sample solutions are accommodated at the probe region, and the local depletion around the sensing area is even worse for shallower channels.

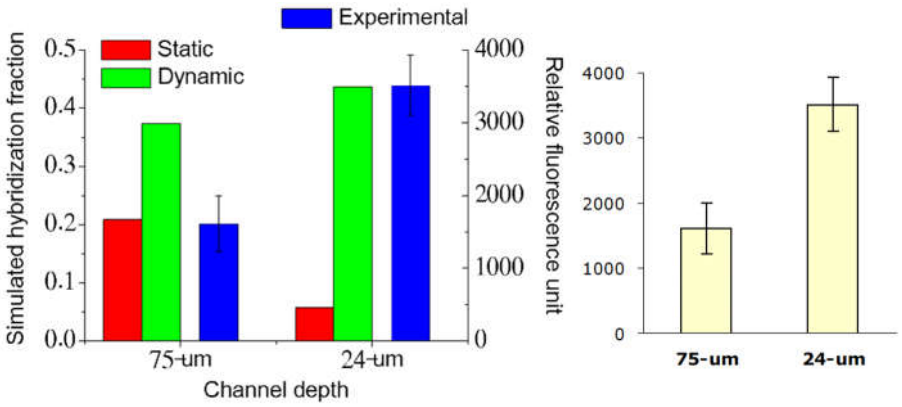

Figure 6. The effect of channel height on hybridization performance. (**a**) The simulated results: static (red), flow (green), and experimental (blue), and (**b**) experimental data (same as blue in a) for the hybridization fractions are obtained in microchannels of 2 different depths (75 μm and 24 μm). The samples are 10 nM and 1 μL. The hybridization times are 3 min. and 30 min. for the flow method and static method, respectively. The *Pe* number of flows in both types of microchannels is 1000.

4. Conclusions

The development of microfluidic DNA microarray technology would largely benefit from theoretical and numerical modelling of the performance-limiting factors, as well as system modelling and optimization of established microfluidic architectures. Our results highlight the importance of incorporating physicochemical factors and microchip parameters in both the design and the data analysis of microfluidic DNA microarrays. Through dimensional analysis and numerical simulations, we demonstrate that (i) convective transport is an efficient way to enhance the kinetics of diffusion-limited hybridization; (ii) the detection range of a DNA microarray is predictable with the proposed model; (iii) fast flow rate is not necessary and a *Pe* number of 10 is high enough to eliminate the diffusion limitation; (iv) low probe coverage facilitates surface reaction but limits hybridization capacity; (v) beside thermodynamic data of DNA duplex formation, kinetic data should be used for the prediction of hybridization fraction, especially for short-time flow hybridization. The proposed

 doi:10.20944/preprints202602.1306.v1

model could be extended for the design and characterization of all relevant microfluidic device prototypes involving surface reactions.

Author Contributions: conceptualization, CHL, LW; methodology, CHL, LW, PS; formal analysis, LW, PS; investigation, LW, PS; resources, PL; writing-original, LW, PS, CHL, writing-review, PS, LW, CHL; supervision, CHL; project admin, CHL; funding acquisition, CHL.

Funding: Funding by NSERC of Canada as said in the paper, grant number is RGPIN-2022-03320

Institutional Review Board Statement: Not applicable.

Informed Consent Statement: Not applicable.

Data Availability Statement: No new data were created or analyzed in this study. Data sharing is not applicable to this article.

Acknowledgments: We gratefully acknowledge financial support from the Natural Sciences and Engineering Research Council (NSERC) of Canada for a Discovery Grant. We also thank Dr. Dipankar Sen for the use of the confocal laser fluorescent scanner.

Conflicts of Interest: The authors declare no conflict of interest.

References

1. Southern, E.; Mir, K.; Shchepinov, M. *Nat. Genet.* **1999**, *21*, 5-9.
2. Bowtell, D.; Sambrook, J. DNA microarrays : a molecular cloning manual; Cold Spring Harbor Laboratory Press: Cold Spring Harbor, N.Y., **2003**.
3. Kim, J. H. S.; Marafie, A.; Jia, X. Y.; Zoval, J. V.; Madou, M. J. *Sensor Actuat B-Chem* **2006**, *113*, 281-289.
4. Benn, J. A.; Hu, J.; Hogan, B. J.; Fry, R. C.; Samson, L. D.; Thorsen, T. *Anal. Biochem*. **2006**, *348*, 284-293.
5. Wang, L.; Li, P. C. H.; Yu, H. Z.; Parameswaran, A. M. *Anal. Chim. Acta* **2008**, *610*, 97-104.
6. Britten, R. J.; Davidson, E. H. *Proc. Natl. Acad. Sci. U. S. A.* **1976**, *73*, 415-419.
7. Wetmur, J. G.; Davidson, N. J. *Mol. Biol*. **1968**, *31*, 349-370.
8. Schuck, P.; Minton, A. P. *Anal. Biochem*. **1996**, *240*, 262-272.
9. Vijayendran, R. A.; Ligler, F. S.; Leckband, D. E. *Anal. Chem*. **1999**, *71*, 5405-5412.
10. Myszka, D. G.; He, X.; Dembo, M.; Morton, T. A.; Goldstein, B. *Biophys. J*. **1998**, *75*, 583-594.
11. Kusnezow, W.; Syagailo, Y. V.; Ruffer, S.; Klenin, K.; Sebald, W.; Hoheisel, J. D.; Gauer, C.; Goychuk, I. *Proteomics* **2006**, *6*, 794-803.
12. Leckband, D. E.; Vijayendran, R. A. *Anal. Chem*. **2001**, *73*, 471-480.
13. Schuck, P. Annu. Rev. Biophys. *Biomol. Struct*. **1997**, *26*, 541-566.
14. Blair, S.; Bishop, J.; Chagovetz, A. M. *Biophys. J*. **2008**, *94*, 1726-1734.
15. Bishop, J.; Blair, S.; Chagovetz, A. *Biosens. Bioelectron*. **2007**, *22*, 2192-2198.
16. Axelrod, D.; Wang, M. D. *Biophys. J*. **1994**, *66*, 588-600.
17. Chan, V.; Graves, D. J.; McKenzie, S. E. *Biophys. J*. **1995**, *69*, 2243-2255.
18. Chan, V.; Graves, D. J.; Fortina, P.; McKenzie, S. E. *Langmuir* **1997**, *13*, 320-329.
19. Singh, R.; Nitsche, J.; Andreadis, S. T. *Ann. Biomed. Eng*. **2009**, *37*, 255-269.
20. Pappaert, K.; Van Hummelen, P.; Vanderhoeven, J.; Baron, G. V.; Desmet, G. *Chem. Eng. Sci*. **2003**, *58*, 4921-4930.
21. Gadgil, C.; Yeckel, A.; Derby, J. J.; Hu, W. S. J. *Biotechnol*. **2004**, *114*, 31-45.
22. Erickson, D.; Li, D. Q.; Krull, U. J. *Anal. Biochem*. **2003**, *317*, 186-200.
23. Zimmermann, M.; Delamarche, E.; Wolf, M.; Hunziker, P. *Biomed Microdevices* **2005**, *7*, 99-110.
24. Squires, T. M.; Messinger, R. J.; Manalis, S. R. Nat. *Biotechnol*. **2008**, *26*, 417-426.
25. Gervais, T.; Jensen, K. F. *Chem. Eng. Sci*. **2006**, *61*, 1102-1121.
26. Pascault, J. R.; Zhou, H. S. *Chem. Eng. Commun*. **2008**, *195*, 167-186.
27. Berthier, J.; Silberzan, P. Microfluidics for biotechnology; 2nd ed.; Artech House: Boston, U. S. A., **2010,** Ch 1, 1-17.

 doi:10.20944/preprints202602.1306.v1

28. Pappaert, K.; Desmet, G. J. *Biotechnol*. **2006**, *123*, 381-396.
29. Wang, L. Q.; Lu, Z. K. *Proceedings of International Symposium on Biophotonics, Nanophotonics and Metamaterials* Oct 16-18, **2006**, 128-130.
30. Wang, L.; Li, P. C. H. J. *Agric. Food Chem*. **2007**, *55*, 10509-10516.
31. Watterson, J. H.; Piunno, P. A. E.; Wust, C. C.; Krull, U. J. *Langmuir* **2000**, *16*, 4984-4992.
32. Peterson, A. W.; Heaton, R. J.; Georgiadis, R. M. *Nucleic Acids Res*. **2001**, *29*, 5163-5168.
33. Jayaraman, A.; Hall, C. K.; Genzer, J. J. *Chem. Phys*. **2007**, *127*, 144912.
34. Gong, P.; Levicky, R. Proc. *Natl. Acad. Sci. U. S. A*. **2008**, *105*, 5301-5306.
35. Gong, P.; Harbers, G. M.; Grainger, D. W. *Anal. Chem*. **2006**, *78*, 2342-2351.
36. Dandy, D. S.; Wu, P.; Grainger, D. W. Proc. *Natl. Acad. Sci. U. S. A*. **2007**, *104*, 8223-8228.
37. Studier, F. W. J. *Mol. Biol*. **1969**, *41*, 199-209.
38. Okahata, Y.; Kawase, M.; Niikura, K.; Ohtake, F.; Furusawa, H.; Ebara, Y. *Anal. Chem*. **1998**, *70*, 1288-1296.
39. SantaLucia, J.; Hicks, D. *Annu. Rev. Biophys. Biomol. Struct*. **2004**, *33*, 415-440.
40. Garrett, R.; Grisham, C. M. Biochemistry; 2nd ed.; Saunders College Pub.: Fort Worth, **1999**, Ch 30, 984-1013.
41. Le Berre, V.; Trevisiol, E.; Dagkessamanskaia, A.; Sokol, S.; Caminade, A. M.; Majoral, J. P.; Meunier, B.; Francois, J. *Nucleic Acids Res*. **2003**, *31*, e88.
42. Michel, W.; Mai, T.; Naiser, T.; Ott, A. *Biophys. J*. **2007**, *92*, 999-1004.
43. Delamarche, E.; Juncker, D.; Schmid, H. *Adv. Mater*. **2005**, *17*, 2911-2933.
44. Squires, T. M.; Quake, S. R. *Rev Mod Phys* **2005**, *77*, 977-1026.
45. Raynal, F.; Plaza, F.; Beuf, A.; Carriere, P.; Souteyrand, E.; Martin, J. R.; Cloarec, J. P.; Cabrera, M. *Phys. Fluids* **2004**, *16*, L63-L66.
46. Noerholm, M.; Bruus, H.; Jakobsen, M. H.; Telleman, P.; Ramsing, N. B. *Lab. Chip* **2004**, *4*, 28-37.
47. Lee, H. H.; Smoot, J.; McMurray, Z.; Stahl, D. A.; Yager, P. *Lab. Chip* **2006**, *6*, 1163-1170.
48. Liu, J.; Williams, B. A.; Gwirtz, R. M.; Wold, B. J.; Quake, S. *Angew Chem Int Edit* **2006**, *45*, 3618-3623.
49. Parsa, H.; Chin, C. D.; Mongkolwisetwara, P.; Lee, B. W.; Wang, J. J.; Sia, S. K. *Lab. Chip* **2008**, *8*, 2062-2070.
50. Phillips, C.; Jakusch, M.; Steiner, H.; Mizaikoff, B.; Fedorov, A. G. *Anal. Chem*. **2003**, *75*, 1106-1115.
51. Wang, L.; Li, P. C. H. *Anal. Biochem*. **2010**, *400*, 282-288.
52. Hofmann, O.; Voirin, G.; Niedermann, P.; Manz, A. *Anal. Chem*. **2002**, *74*, 5243-5250.
53. Mocanu, D.; Kolesnychenko, A.; Aarts, S.; Troost-Dejong, A.; Pierik, A.; Vossenaar, E.; Stapert, H. *J. Biotechnol*. **2009**, *139*, 179-185.
54. Yamashita, K.; Miyazaki, M.; Yamaguchi, Y.; Nakamura, H.; Maeda, H. *Lab. Chip* **2008**, *8*, 1171-1177.
55. Chung, Y. C.; Lin, Y. C.; Shiu, M. Z.; Chang, W. N. T. *Lab. Chip* **2003**, *3*, 228-233.
56. Bajcsy, P. *Computer Society of India Communications*, 2007, 30, 18–23.
57. Pappaert, K.; Ottevaere, H.; Thienpont, H.; Van Hummelen, P.; Desmet, G. *Biotechniques* **2006**, *41*, 609-616.
58. Moran-Mirabal, J. M.; Tan, C. P.; Orth, R. N.; Williams, E. O.; Craighead, H. G.; Lin, D. M. *Anal. Chem*. **2007**, *79*, 1109-1114.
59. Li, Q. H.; Fraley, C.; Bumgarner, R. E.; Yeung, K. Y.; Raftery, A. E. *Bioinformatics* **2005**, *21*, 2875-2882.
60. Deegan, R. D.; Bakajin, O.; Dupont, T. F.; Huber, G.; Nagel, S. R.; Witten, T. A. *Nature* **1997**, *389*, 827-829.
61. Blossey, R.; Bosio, A. *Langmuir* **2002**, *18*, 2952-2954.
62. Chen, H.; Wang, L.; Li, P. C. H. *Lab. Chip* **2008**, *8*, 826-829.
63. Xing Yue (Larry) Peng, Paul C.H. Li, Hua-Zhong (Hogan) Yu, Ash M. Parameswaran, Wa Lok (Jacky) Chou, *Sens. Actuators* B, **2007**, *128*, 64-69.
64. Lin Wang and Paul C.H. Li, *Biomicrofluidics*, **2010**, *4*, 032209,
65. Abootaleb Sedighi and Paul C.H. Li. *Anal. Biochem*. **2014**, *448*, 58-64
66. Abootaleb Sedighi, Paul C. H. Li, Idah C. Pekcevik, and Byron D. Gates, *ACS Nano*, **2014**, *8*, 6765-6777.